MAVEN SWEA Version 4 Data Products – What's New?

D. L. Mitchell (SWEA Lead)

December 5, 2016
January 6, 2017 (revised)

Introduction

During the course of the MAVEN mission, in-flight calibrations and cross calibrations have resulted in a better understanding of the SWEA instrument response in both energy and angle, as well as its overall sensitivity relative to SWIA, STATIC, LPW, and NGIMS. These calibrations include regularly scheduled activities, during which the instrument is commanded to scan for the optimal microchannel plate (MCP) bias voltage and to alter its energy sweep table to probe the energy dependence of the instrument sensitivity. There are also calibrations that can be performed on science data under the appropriate conditions.

Microchannel Plate Gain Variations

Commanded in-flight calibration sequences, performed monthly, consist of two parts. The first part is designed to optimize the MCP bias voltage. As charge is extracted from the MCP during normal use, the gain gradually drops. This loss of gain can be monitored by cross calibrations with SWIA and STATIC, which are in turn calibrated against LPW measurements of the ionospheric plasma frequency, which provides an absolute calibration. The SWEA MCPs have channels with an 80:1 (length-to-diameter) aspect ratio. This is twice the aspect ratio of the 40:1 MCPs used by SWIA and STATIC. One consequence of this difference is that the SWEA MCPs require a larger bias voltage (currently 2450 V) to achieve the same gain per plate as for SWIA and STATIC (~1800 V). Additionally, there is a larger variation of gain with time, which is accounted for in the data reduction by a time-varying efficiency factor.

The MCP efficiency variation is determined by cross calibrating with SWIA in the upstream solar wind. In this region, ions (mainly H^+ and He^{++}) are beamed primarily along the Mars-Sun line so that the distribution is entirely within SWIA's field of view (FOV), which allows a reliable estimate of the solar wind ion density. At the same time, SWEA measures the solar wind electron distribution over 80% of the sky. To estimate the total electron density, we calculate the density moment of the measured distribution, corrected for spacecraft potential, as described in Mitchell et al. (2016), under the assumption that the part of the distribution within the instrument's blind spots is not too different from the measured part of the distribution. (Specifically, we assume that the energy flux within the blind spots is equal to the average energy flux measured over the rest of the sky.) This is a reasonable approximation for the solar wind core population, which typically accounts for >90% of the total density (see Mitchell *et al.*, 2016, Fig. 21). The solar wind halo population, which accounts for the remainder of the density, is at times strongly beamed along the magnetic field direction, so for best results, we choose times when this beamed distribution is within the instrument's field of view. Comparing the total ion density with the total electron density, assuming charge neutrality, provides an

estimate of relative sensitivities of SWEA and SWIA. Numerous cross calibrations over the course of the mission reveal the variation of SWEA's MCP efficiency with time (Fig. 1).

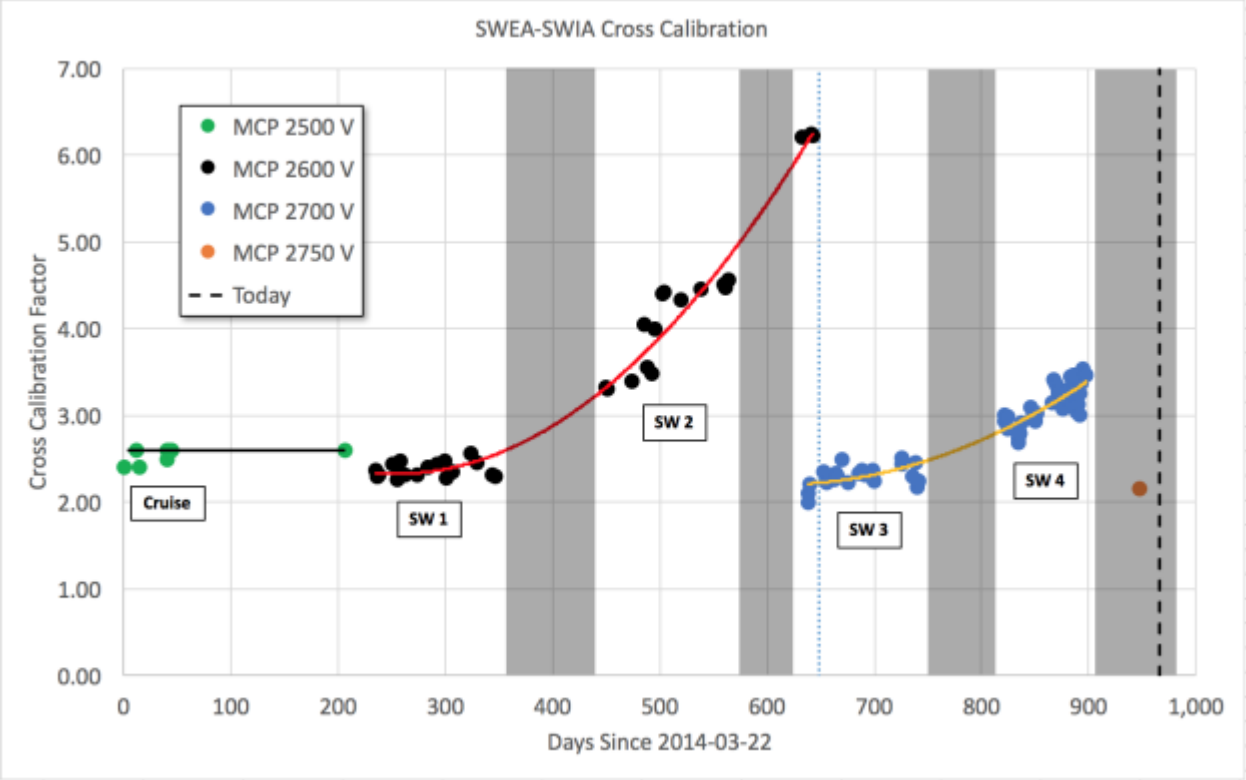

Figure 1: Cross calibration factor (ion density divided by electron density) in the upstream solar wind. Symbols indicate cross calibration measurements, with a color that corresponds to SWEA's MCP bias (see key inset). Solar wind calibration periods 1-4 are separated by intervals during which the orbit was entirely downstream of the bow shock (shaded regions). The red and orange curves are 2nd order polynomial fits to the data. A single value (black line) is chosen for cruise and early commissioning. The single data point for a 2750-V MCP bias (far right) is based on comparing sheath electron fluxes immediately before and after the MCP bias was increased from 2700 to 2750 V.

The cross calibration factor shown in Fig. 1 is relative to the expected sensitivity based on electrostatic optics simulations, with an assumed 70% MCP efficiency, and ground calibrations at IRAP (see Mitchell et al. 2016). The observed sensitivity based on cross calibration with SWIA appears to be ~2 times smaller than expected when the MCP bias is optimized.

When the gain drops by a factor of ~2, we command the MCP bias voltage to a higher value. This restores the gain to its optimal value, and the gradual gain drift begins again. The large gain variation during solar wind period 2 caught us by surprise until we appreciated the significant differences in the gain behavior of 80:1 and 40:1 MCPs. Polynomial fits through the measured values are used to adjust SWEA's sensitivity to match that of SWIA. **Note that this is a relative correction.** The absolute sensitivity further depends on cross calibrations between SWIA and STATIC in the magnetosheath, and finally between STATIC and LPW in the ionosphere. At present, the cross calibration between these four instruments is believed to be accurate to about 20%.

Angular Sensitivity

Cross calibration with SWIA provides the overall MCP gain variation with time, but this variation need not be uniform around the MCP. In addition, there are three corrections to the angular sensitivity that do not depend on time. First, there are a few solid angle bins that are partially (< 30%) blocked by the spacecraft but otherwise scientifically useful. (Fully blocked bins are masked in the SWEA L2 data products.) Second, there are "edge effects" at the maximum upward and downward deflections that are caused by impingement on the FOV by the deflectors themselves. Finally, the transparency of the toroidal entrance grids varies with elevation by about 15%, depending on the alignment of the holes between the inner and outer grids.

The actual angular sensitivity, including all of these effects, can be determined from science data under the approximation that the electron angular distribution is symmetric about the magnetic field direction (gyrotropic) in the plasma rest frame. This calibration is performed upstream of the Mars bow shock during steady solar wind conditions. We transform SWEA 3D (energy-azimuth-elevation) distributions to the plasma rest frame using measurements of the solar wind bulk flow velocity from SWIA. We choose time intervals during which the magnetic field direction is nearly constant, which allows us to average distributions over several minutes to improve statistics without smearing the pitch angle mapping around the FOV. We choose an energy of 125 eV, corresponding to the solar wind halo population, which is usually beamed along the magnetic field. Electrons at this energy are not strongly affected by the spacecraft potential, which is typically +7 Volts in the solar wind. In the worst case, electrons passing close to the spacecraft on their way to SWEA are accelerated by this potential in a direction orthogonal to their original path, resulting in a maximum deflection of 13°, which is about half the angular bin width. As the magnetic field direction varies from one calibration period to the next, the beamed halo distribution is incident on different parts of the FOV. Occasionally, the beam overlaps the FOV edge or is partially occulted by the spacecraft, which allows us to map the sensitivity in these directions.

Calibrations are performed in the four solar wind periods identified in Fig. 1 (SW1 – SW4). Figures 2-4 shows the results for the first three periods. Bins 19 and 20 are partially blocked by the spacecraft, which reduces the sensitivity in those directions by about 20%. Bins 80-95 (maximum upward deflection) are systematically low because of impingement on the field of view by the upper deflector. This effect is less pronounced for the maximum downward deflection because there is less impingement by the lower deflector, in agreement with simulations. The angular sensitivity maps for solar wind periods 1 and 3, measured one year apart, are nearly the same (Fig. 4). Thus, increasing the MCP bias to restore the optimal gain also restores the angular sensitivity to its previous state. This indicates that variations in the angular sensitivity with time depend primarily on MCP gain. Interpolation across the periods without solar wind coverage (shaded regions in Fig. 1) is performed linearly with respect to gain (polynomial fits in Fig. 1).

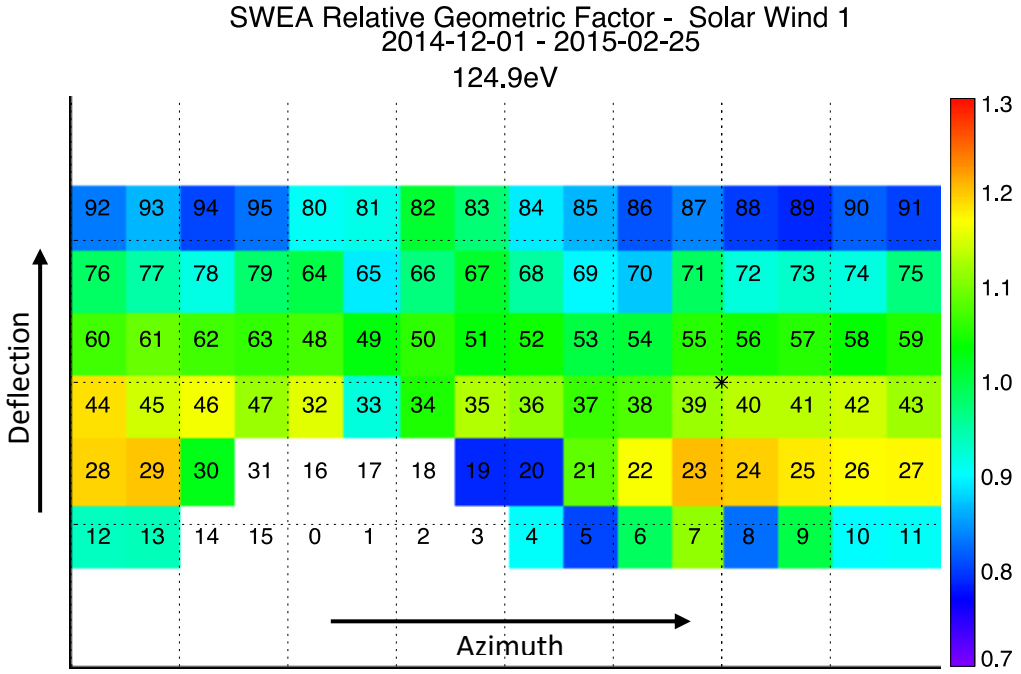

Figure 2: Relative angular sensitivity during solar wind period 1. There are 16 azimuths for each of 6 deflections for a total of 96 solid angle bins, each ~20° on a side. Bins that are fully blocked by the spacecraft have no color.

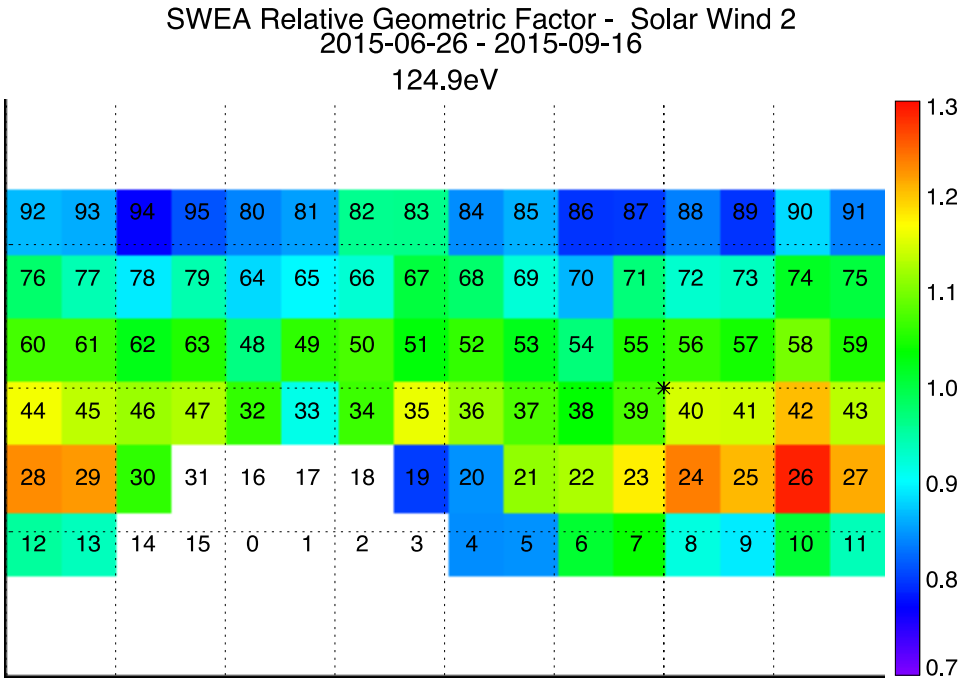

Figure 3: Relative angular sensitivity during solar wind period 2. As the MCP gain drops, the magnitude of the variation around the FOV increases, although the same overall trends are present.

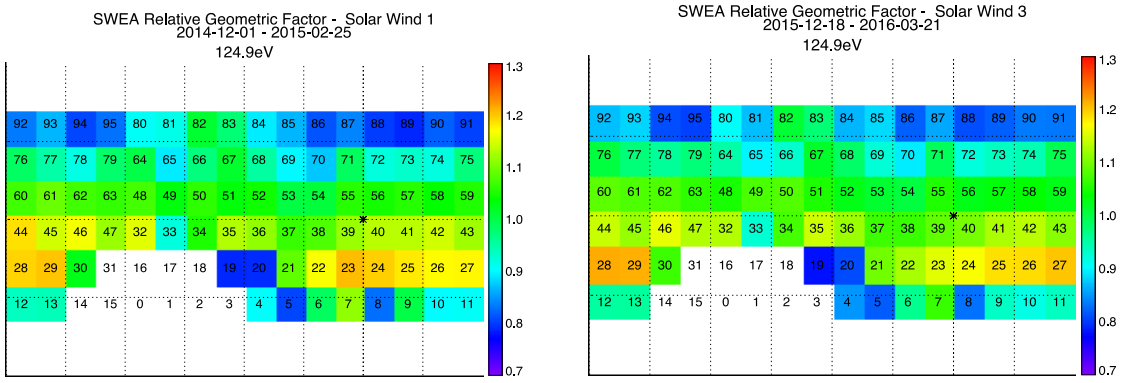

Figure 4: Comparison of the angular sensitivity during solar wind periods 1 and 3. Prior to both periods, the MCP gain was optimized (see Fig. 1). There is close agreement (within a few percent) between the two calibrations obtained with similar gains but taken one year apart.

Low-Energy Sensitivity

During another part of the monthly commanded calibration sequences, the instrument alternates between two energy sweep tables several times while taking measurements in the magnetosheath. Both sweep tables are stored in SWEA on-board memory, so changing between them takes place immediately (more precisely, during the 0.05-sec gap between measurement cycles). One sweep table is the nominal table that has been used for nearly all science data to date. The other table enables V_0, which places a potential between the inner and outer toroidal grids (see Mitchell *et al.* 2016). This potential decelerates incoming electrons so that they pass through the instrument's internal electrostatic optics at a lower energy than they otherwise would. Since the electron phase space density [cm^{-3} $(km/s)^{-3}$] is conserved across electrostatic potentials, we can measure the same phase space density over two different instrumental energy ranges. This allows us to calibrate the variation of sensitivity with energy from 3 to 75 eV, with the assumption that the true phase space density does not vary significantly in the time it takes to measure the distribution with both sweep tables. Toggling several times between sweep tables allows us to assess the validity of this assumption.

It is useful to consider the electron energy at three locations: far from the spacecraft (E), after crossing the spacecraft potential but before entering the instrument (E'), and after passing through both toroidal grids (E''). When enabled, the deceleration potential across the toroidal grids (V_0) is set in the sweep table to be proportional to the acceptance energy inside the instrument: $V_0 = -E''/2$. By conservation of phase space density across the toroidal grids, this mode reduces the effective sensitivity by a constant factor of 4/9 up to a maximum energy of $E'' = 50$ eV (since the maximum value of V_0 is -25 V). This corresponds to an energy just outside of the toroidal grids of $E' = 75$ eV. For higher energies, we hold V_0 constant at its maximum value of -25 V, so that the sensitivity smoothly returns to its nominal value. A sample calibration is shown in Figs. 5-6.

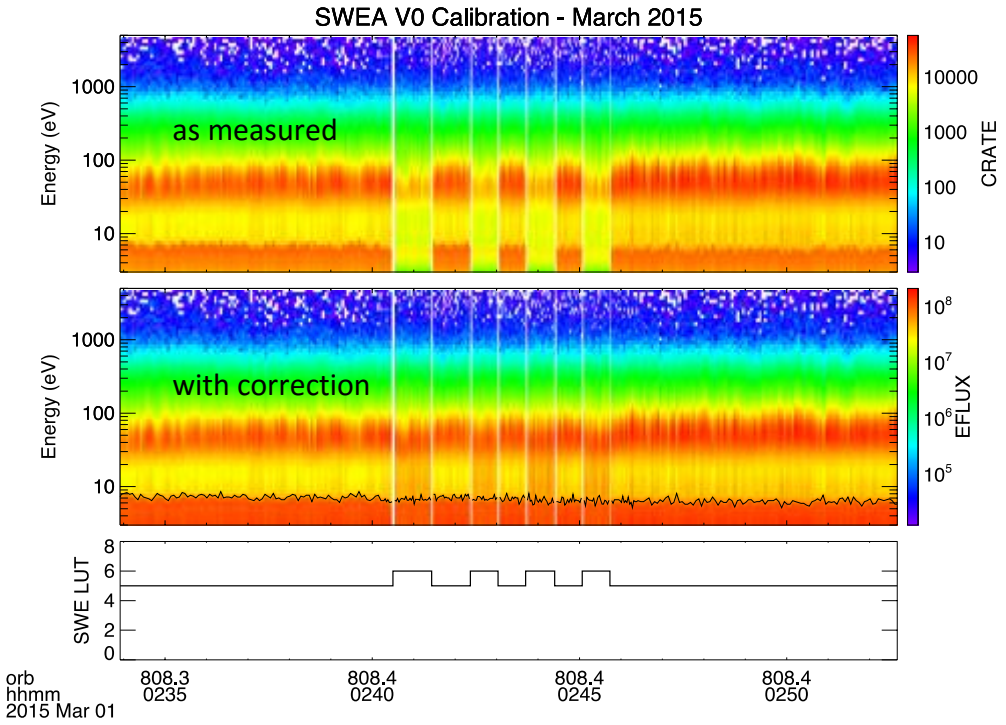

Figure 5: Alternating sweep tables while taking measurements in the magnetosheath. Sweep table 5 is nominal ($V_0 = 0$) and table 6 enables the potential across the toroidal grids ($V_0 = -E''/2$). The top panel is the measured count rate, corrected only for dead time, and the second panel applies the calibration shown in Fig. 6 with $K_e = 3.1$. The bottom panel shows the toggling between sweep lookup tables (LUTs), as recorded in housekeeping.

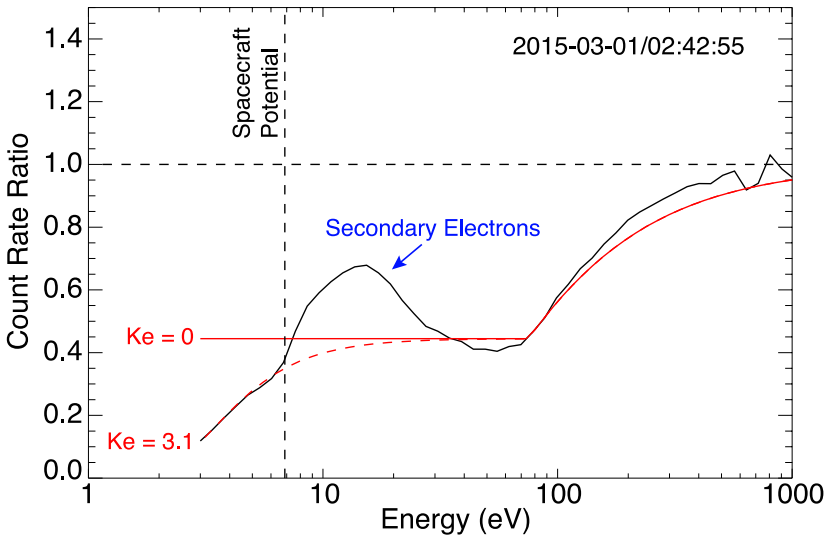

Figure 6: Low energy calibration derived from alternating between two sweep tables (Fig. 5). The quantity shown by the solid black line is the ratio of the count rate with $V_0 = -E''/2$ (sweep table 6) to the count rate with $V_0 = 0$ (sweep table 5). Both signals are referenced to the energy just outside the instrument (E', abscissa scale). The solid and dashed red curves are modeled responses (see text).

The ratio of the measured count rates with V_0 enabled and disabled is shown by the black line. The solid red curve shows the theoretical instrument response based on conservation of phase space density. The measured count rate ratio deviates significantly from the theoretical response below energies (E') of 30 eV. First, there is an increased count rate ratio from 8 to 30 eV, which is caused by secondary electrons created by out-of-band primary electrons that impact the hemispheres above the exit grid. These secondary electrons are produced inside the instrument and generate counts in addition to the signal from primary electrons that pass through the electrostatic optics.

At energies below 10 eV, the count rate ratio falls off rapidly with decreasing energy. Empirically, this fall-off has the functional form:

$$C = \exp(-(K_e/E'')^2) \quad (1)$$

where K_e is a constant. When K_e = 0, the correction factor is unity. Otherwise, there is a steep drop in sensitivity for energies (E'') less than a few times K_e (Fig. 6, dashed red curve). This behavior corresponds to an analyzer that is slightly "detuned", such that the acceptance energy varies with position inside the analyzer. This could result from a variation in the work function across the analyzer's hemispheres, so that a voltage applied to the inner hemisphere does not provide a uniform potential just above the surface. At high energies, where variations in the work function are much smaller than the analyzer voltage, the effect is unnoticeable, but at low energies, the correction can be significant.

Another method of calibrating the low-energy sensitivity can be performed in the ionosphere when the spacecraft potential varies significantly. The spacecraft potential depends in part on its orientation with respect to the ram flow as it goes through periapsis. When the flow is from the side (orthogonal to the high gain antenna axis), there is significant ion ram current onto conducting surfaces of the spacecraft, which nearly balances the electron current that is incident from all directions. In this case, the spacecraft charges only a few volts negative to repel a small part of the electron flux and thus achieve zero net current. However, on some orbits, the ram flow is incident mostly on the fronts of the solar panels and the antenna radome. Since those non-conducting surfaces do not share ion ram current with the rest of the spacecraft, the conducting parts of the spacecraft (to which the instruments are grounded) must charge more negative to repel a larger fraction of the ionospheric electron flux. This effect is more pronounced at low altitudes, where ions are colder (and more collimated) because of collisional coupling to the neutral atmosphere.

The ionospheric photoelectron energy spectrum has discrete peaks at 23 and 27 eV, which result from ionization of CO_2 and O by the intense 30.4-nm He-II line in the solar spectrum. The shape of the photoelectron spectrum from ~15 to 50 eV does not change significantly with altitude from 150 to 300 km, which we verified empirically on orbits where the spacecraft potential did not vary significantly (ram flow from the side). As the spacecraft potential goes more negative, the measured positions of the He-II peaks shift to lower energies, since these

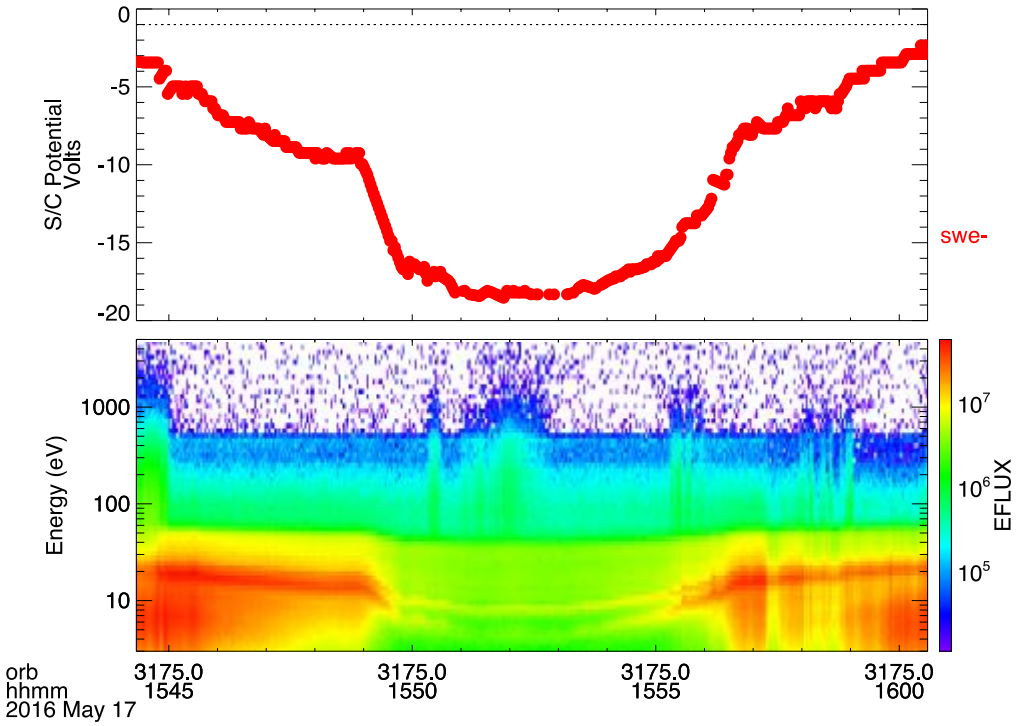

Figure 7: Spacecraft potential (top) as inferred from the measured energies of the He-II photoelectron features at 23 and 27 eV (bottom). Differential energy flux (eV/cm^2-s-ster-eV) is shown as a function of energy just outside the toroidal grids (E'). Between 15:49 and 15:56, the He-II features are resolved (faint yellow arcs).

electrons are decelerated before entering the instrument (Fig. 7). Again, we can use the principle of phase space conservation to compare spectra measured with different spacecraft potentials. Essentially, the He-II peaks are measured over a range of internal energies (E'') as the spacecraft potential varies. Transforming to the plasma frame many Debye lengths away from the spacecraft (using the potential determined from the amount of the peak shift), the overall shape of the spectra should be the same from 15 to 50 eV. Any deviations from this must result from variations in the sensitivity with energy.

Figure 8 shows photoelectron energy spectra measured at five different values of the spacecraft potential, ranging from −5 to −14 Volts. All spectra have been transformed to the plasma frame and then corrected for detuning using Eq. 1 with three different values of K_e. When K_e is too small (left two panels), the spectra do not agree at energies below 20 eV. When K_e is increased to 3, the spectra very nearly line up. The optimal value of K_e for this case is 2.9, which agrees well with the value of K_e derived from alternating the sweep table. Note that the flux levels for all spectra are as measured – they have not been shifted vertically to line up. Agreement between the spectra is achieved entirely by varying K_e.

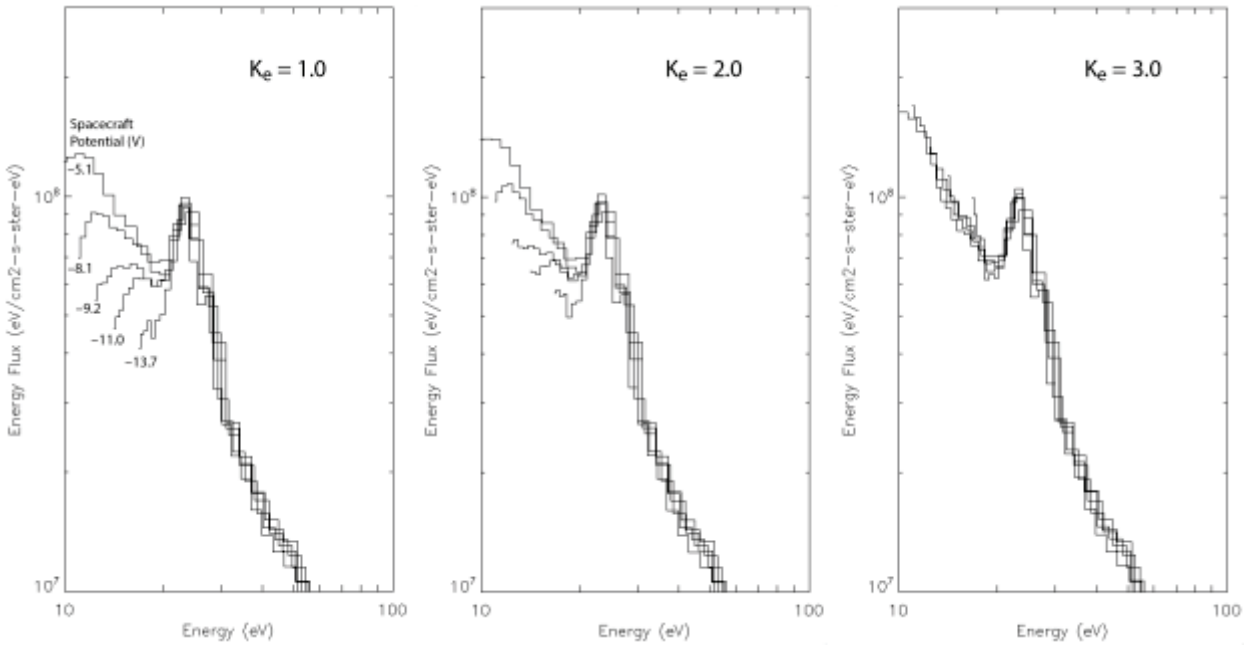

Figure 8: Ionospheric photoelectron spectra in the vicinity of the He-II feature at 23-27 eV. These spectra were measured at different times on May 17, 2015, as the spacecraft potential varied (see Fig. 7). All spectra are transformed to the plasma frame (abscissa energy scale). The three panels show the same five spectra corrected for detuning using Eq. 1 with different values of K_e.

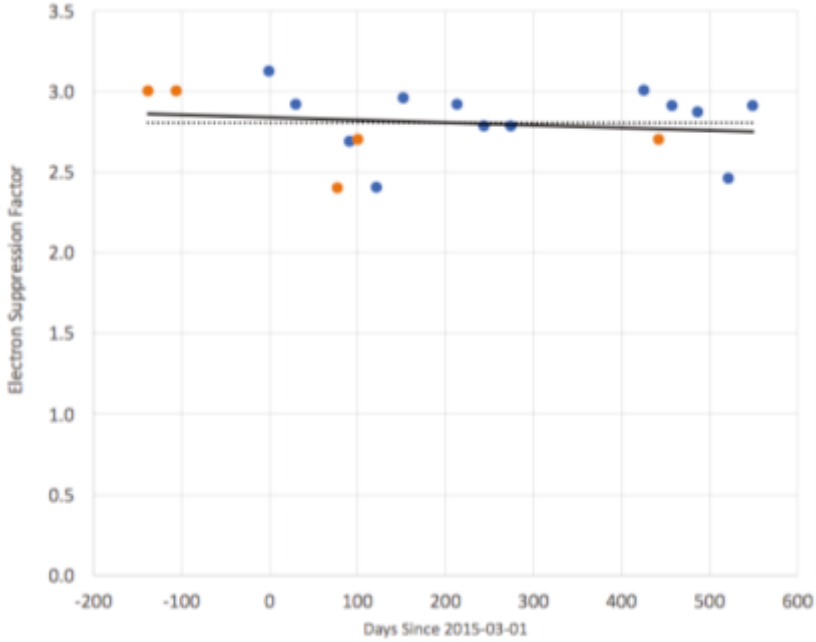

Figure 9: Estimated values of K_e over the mission to date, based on alternating sweep tables (blue symbols) and ionospheric photoelectron spectra (orange symbols). The best-fit linear trend is shown by the solid line. The average of all estimates (2.8 ± 0.2) is shown by the dotted line.

Figure 9 shows estimates of K_e derived from monthly calibrations (alternating sweep tables) and from photoelectron spectra measured during periods when the spacecraft potential varied. The earliest estimate is on October 14, 2014, during the commissioning phase, just prior to the start of regular science operations. Monthly calibrations began on March 1, 2015. Both methods are in good agreement. A linear fit through the data is indistinguishable from the mean value of 2.8 ± 0.2. The lack of a trend indicates that detuning has likely been present since launch.

Implementation

The calibrations described above are implemented within the existing L2 data format. The polynomial curves shown in Fig. 1 provide the correction to the overall sensitivity as a function of time. (Additional polynomial fits will be provided for future solar wind calibration periods.) The CDF variable GEOM_FACTOR remains unchanged in order to maintain a record of the pre-launch calibration, as described in Mitchell *et al.* 2016. The cross calibration shown in Fig. 1 is implemented with an overall multiplicative factor to G_ENGY, with one correction factor per UT day. The correction for "detuning" at low energies is calculated from Eq. 1 with $K_e = 2.8$ and applied to G_ENGY. At present, the same correction is applied throughout the mission, although we will continue to monitor the calibration and search for time dependence. The relative angular sensitivity shown in Figs. 2-4 is applied to the existing angular correction terms in the 3D and PAD data products: G_AZIM, G_ELEV, and G_PA.

Reference

Mitchell, D. L., C. Mazelle, J.-A. Sauvaud, J. J. Thocaven, J. Rouzaud, A. Federov, P. Rouger, D. Toublanc, E. Taylor, D. Gordon, M. Robinson, S. Heavner, P. Turin, M. Diaz-Aguado, D. W. Curtis, R. P. Lin, and B. M. Jakosky, The MAVEN Solar Wind Electron Analyzer, *Space Sci. Rev.* **200**, Issue 1-4, pp. 495-528, 2016.